



CHORUS

This is the accepted manuscript made available via CHORUS. The article has been published as:

Role of Ce^{4+} in the Scintillation Mechanism of Codoped $\text{Gd}_3\text{Ga}_3\text{Al}_2\text{O}_{12}:\text{Ce}$

Yuntao Wu, Fang Meng, Qi Li, Merry Koschan, and Charles L. Melcher

Phys. Rev. Applied **2**, 044009 — Published 17 October 2014

DOI: [10.1103/PhysRevApplied.2.044009](https://doi.org/10.1103/PhysRevApplied.2.044009)

1 **The role of Ce⁴⁺ in scintillation mechanism: Codoped Gd₃Ga₃Al₂O₁₂:Ce**

2 Yuntao Wu^{*a,b,c}, Fang Meng^{a,b}, Qi Li^{*,d}, Merry Koschan^b, Charles L. Melcher^{a,b}

3 ^a *Scintillation Materials Research Center, University of Tennessee, Knoxville, Tennessee 37996, USA*

4 ^b *Department of Materials Science and Engineering, University of Tennessee, Knoxville, Tennessee*
5 *37996, USA*

6 ^c *Shanghai Institute of Ceramics, Chinese Academy of Sciences, Jiading, Shanghai 201899, P.R. China*

7 ^d *Department of Physics, Wake Forest University, Winston-Salem, NC 27109, USA*

8 **Abstract** To control the time response performance of widely used cerium-activated scintillators in
9 cutting-edge medical imaging devices, such as time-of-flight positron emission tomography, a
10 comprehensive understanding of the role of Ce valence states, especially stable Ce⁴⁺, in the scintillation
11 mechanism is essential. However, despite some progress made recently, an understanding of the
12 physical processes involving Ce⁴⁺ is still lacking. The aim of this work is to clarify the role of Ce⁴⁺ in
13 scintillators by studying Ca²⁺ codoped Gd₃Ga₃Al₂O₁₂:Ce (GGAG:Ce). By using a combination of
14 optical absorption spectra and X-ray absorption near edge spectroscopies, the correlation between Ca²⁺
15 codoping content and Ce⁴⁺ fraction is seen. The energy level diagrams of Ce³⁺ and Ce⁴⁺ in the
16 Gd₃Ga₃Al₂O₁₂ host have been established by using theoretical and experimental methods, which
17 indicate a higher position of the 5d₁ state of Ce⁴⁺ in the forbidden gap in comparison to that of Ce³⁺.
18 Underlying reasons for the decay time acceleration resulting from Ca²⁺ codoping are revealed, and the
19 physical processes of the Ce⁴⁺ emission model is proposed and further demonstrated by
20 temperature-dependent radioluminescence spectra under X-ray excitation.

21 **Kew words:** Ce⁴⁺, scintillator, codoping, luminescence.

22 Corresponding author email: ywu52@utk.edu, caswyt@hotmail.com (Y.T. Wu), liq9@wfu.edu (Q. Li).

23

24 I. INTRODCUTION

25 Positron emission tomography (PET), as a highly sensitive non-invasive medical imaging
26 technique, is ideally suited for pre-clinical and clinical imaging of cancer biology, which is important to
27 cancer imaging [1]. Inorganic scintillation crystals, as the key components in PET, are utilized to detect
28 γ -rays produced by the annihilation of positrons emitted by injected tracers. The ultimate performance
29 of the PET camera strongly relies on the physical and scintillation properties of the crystals [2]. So far,
30 the single crystal scintillators for commercial PET cameras are $\text{Bi}_4\text{Ge}_3\text{O}_{12}$ (BGO) [3], $\text{Lu}_2\text{SiO}_5\text{:Ce}$
31 (LSO:Ce) [4], and the $\text{Lu}_{1.8}\text{Y}_{0.2}\text{SiO}_5\text{:Ce}$ (LYSO:Ce) [5]. Significant improvements have made it
32 possible to add the technology of time-of-flight (TOF) to improve the image quality of PET [6]. Among
33 the single crystals used for PET applications, LSO:Ce is the best candidate for TOF-PET application
34 because of the key parameter of short decay time, e.g. 40 ns for LSO:Ce [4]. One requirement for TOF
35 is the best possible coincidence time resolution (CTR), the figure of merit of which should be 200 ps or
36 better [7]. Since excellent timing resolution can best be achieved on a scintillator with faster decay time
37 and higher light yield [8], a divalent ion codoping strategy was applied over the past six years to
38 improve the time response characteristics in trivalent-cation based oxide scintillators such as
39 LSO:Ce,Ca, [9] LYSO:Ce,Ca/Mg [10], and $\text{Lu}_3\text{Al}_5\text{O}_{12}\text{:Ce,Mg}$ (LuAG:Ce,Mg) [11,12] without
40 sacrificing (or even enhancing) the light yield when a low codoping concentration of 0.1 at% was used.
41 Compared with a CTR of 190 ps for LSO:Ce, an even better CTR of 170 ps can be measured on a 0.4
42 at% Ca codoped LSO:Ce single crystal under the same conditions [7], but with relatively lower light
43 yield. Thus, understanding of the fundamental physical processes causing the acceleration of decay
44 kinetics by divalent codoping is essential for designing other promising candidates for TOF-PET
45 application.

46 There are some hypotheses in the literature for the mechanism of decay time shortening as a result
47 of codoping. In LSO:Ce,Ca, a proposed cause was the suppression of the slower emission from the
48 6-oxygen coordinated Ce2 sites and improved chances for migrating charge carriers to be captured by
49 the faster 7-oxygen coordinated Ce1 sites [13]. It has also been ascribed to the reduction of traps acting
50 to slow the scintillation process [14]. Recently, a model of Ce^{4+} ions as an intermediate state in the
51 process leading to a Ce^{3+} excited state was used to explain the decay time acceleration of LYSO:Ce
52 single crystals by Ca^{2+} or Mg^{2+} codoping [10]. Nevertheless, without solid evidence such as
53 observation of $(\text{Ce}^{3+})^*$ excitation emission from a scintillator material in which Ce^{4+} has dominating

54 concentration over Ce^{3+} , the Ce^{4+} emission model is still not firmly proved.

55 The $Gd_3Ga_3Al_2O_{12}:Ce$ (GGAG:Ce) single crystal scintillator was developed as an improvement of
56 the LuAG:Ce scintillator, based on band-gap engineering [15,16] and cerium valence instability [17] by
57 a Ga^{3+} admixture, and energy level positioning by a Gd^{3+} admixture [18,19]. It shows very high light
58 yield of up to 50,000 photons/MeV, which exceeds by 30-40% the light yield value of the best
59 LYSO:Ce scintillators ever reported [20]. A 2 inch diameter GGAG:Ce single crystal was successfully
60 grown at the Furukawa Co. Ltd. in 2012, which was expected to be a promising candidate for use in
61 PET [21]. However, its main decay component of 88 ns [21], a relatively slow time response compared
62 with LSO:Ce, might be a bottleneck that hinders its application. Our recent work has shown that the
63 decay kinetics of GGAG:Ce can be accelerated by codoping with Ca^{2+} ions, though at the expense of
64 light yield [22]. At certain Ca^{2+} codoping concentration, such as 0.1 at%, the scintillation decay time
65 can be shortened to about 46 ns with a light yield of about 40,000 photons/MeV [23], which may pave
66 the way to its PET and TOF-PET applications.

67 Clarifying the role of a Ca^{2+} codopant in $Gd_3Ga_3Al_2O_{12}:Ce$ scintillation kinetics with an eye
68 toward enabling design of advanced compositions for Ce^{3+} activated PET and TOF-PET applications
69 served as a motivation for this work. Here we report the correlation between Ca^{2+} codoping
70 concentration and the Ce^{3+}/Ce^{4+} ratio as determined by optical absorption spectra and X-ray absorption
71 near edge spectroscopy (XANES). By varying the Ca^{2+} codoping concentration, a sample almost
72 completely activated by Ce^{4+} was identified. The related energy level diagram of Ce^{3+} and Ce^{4+} in the
73 GGAG:Ce host was constructed by using the three-parameter experimental method [24] and the
74 DFT+ G_0W_0 theoretical calculation method. The higher position of the lowest $5d_i$ excited state of Ce^{4+}
75 in the forbidden gap in comparison to that of Ce^{3+} was confirmed. Furthermore, a Ce^{4+} emission model
76 is presented and corroborated by temperature-dependent radioluminescence spectra under X-ray
77 excitation. Based on these results, the fundamental origins of the shorter decay time resulting from Ca^{2+}
78 codoping in GGAG:Ce is addressed and compared to the cases of Ca^{2+} or Mg^{2+} codoped LSO:Ce,
79 LYSO:Ce and LuAG:Ce. Experiments on B^{3+} and Ba^{2+} codoped GGAG:Ce single crystals were also
80 done for comparison.

81

82 II. EXPERIMENTAL AND THEORETICAL METHODS

83 Seven GGAG crystals were grown via the Czochralski method. The compositions are given in
 84 TABLE I. All crystals were grown in inductively heated \varnothing 60 mm \times 60 mm iridium crucibles in a
 85 Cyberstar Oxypuller 05-03 Czochralski growth station. Three percent excess Ga was added to an
 86 otherwise stoichiometric melt composition in order to compensate for its volatilization loss from the
 87 melt. In all cases, the dopant and codopant concentrations given refer to the initial starting melt and
 88 calculations were based on the assumption that the dopants substituted for Gd based on atomic size
 89 matching. Note that the dopant concentrations in the finished boules will differ from that in the melt
 90 due to segregation at the solid-liquid interface. The growth atmosphere was flowing nitrogen with a
 91 small fraction of a percent oxygen.

92 **TABLE I.** The concentration of activator and codopants in GGAG melt, the concentration given are
 93 respect to Gd.

| <i>Compositions</i> | <i>Ce concentration (at%)</i> | <i>Codopant concentration (at%)</i> |
|---------------------|-----------------------------------|---|
| GGAG:Ce | 0.2 | - |
| GGAG:Ce,Ca | 0.2 | 0.1 |
| | 0.2 | 0.2 |
| | 0.2 | 0.4 |
| GGAG:Ce,Ba | 0.2 | 0.2 |
| GGAG:Ce,B | 0.2 | 0.2 |

94
 95 Optical absorption spectra were measured with a Varian Cary 5000 UV-VIS- NIR
 96 spectrophotometer in the 200-800 nm range. Photoluminescence (PL) emission and excitation
 97 spectra were measured with a HORIBA Jobin Yvon Fluorolog-3 spectrofluorometer. The
 98 excitation light passed through an excitation monochromator with a 1 nm bandpass to ensure
 99 monochromaticity. Similarly, the emission monochromator was set at a 1 nm bandpass to select
 100 emission light of a specific wavelength. A 450W continuous xenon lamp was used as the
 101 excitation source in emission and excitation spectra.

102 XANES spectra of codoped GGAG:Ce single crystals were recorded at BL14W1, a
 103 wiggler-based beamline in the Shanghai Synchrotron Radiation Facility (SSRF).
 104 Room-temperature measurements were made at the Ce L_{III}-edge (5723 eV), in the fluorescence
 105 mode due to the low cerium content, using a Si (111) double crystal monochromator. The
 106 XANES spectra were recorded in two regions: (1) from 5700 to 5720 eV (pre-edge) every 0.5
 107 eV with 5 s accumulation time per point; (2) from 5720 to 5780 eV (XANES), every 0.5 eV
 108 with 8 s accumulation time per point. The powders were evenly coated on transparent tape for
 109 measurements. The XANES spectra of Ce⁴⁺ and Ce³⁺ standard samples were recorded at the

110 XAFS station of Beijing Synchrotron Radiation Facility (BSRF) and the specific measurement
111 description can be found in Ref. 25. All spectra were normalized in the same way using the
112 Athena software [26].

113 For temperature-dependent radioluminescence spectra, a sample was mounted on a cold
114 finger of the cryostat. The pressure was reduced to 12 mTorr and the sample was measured
115 from 500 K to 40 K to avoid interference from thermoluminescence when irradiated by an
116 X-ray generator (X-ray Model; CMX003) at 35 kV and 0.1 mA.

117 The absolute light yield measurement was recorded by using a pulse processing chain
118 consisting of an Hamamatsu R2059 photomultiplier tube (PMT) operated at $-1500 V_{\text{bias}}$, an
119 Ortec 672 Amp, a Canberra model 2005 pre-Amp and a Tukan 8k multi-channel analyser. The
120 PMT was directly coupled to each sample using mineral oil, and a PTFE-lined dome-shaped
121 reflector with a 50 mm diameter was used to maximize the collection of light. The
122 photoelectron yield of the samples was calculated by using the single photoelectron peak
123 method. Measurements on the samples were made at a gain of 5 with 2 μs shaping time to
124 provide full light integration. The sample was measured for 20 min during its irradiation with a
125 $15 \mu\text{Ci } ^{137}\text{Cs}$ source at a distance of about 20 cm. The reproducibility of light yield is $\pm 5\%$.

126 Electronic structure calculations of bulk GGAG crystals were carried out using the Vienna
127 Ab-initio Simulation Package (VASP) [27,28] with projector augmented wave (PAW)
128 pseudopotentials and generalized gradient approximation exchange-correlation functionals
129 parametrized by Perdew-Burke-Ernzerhof (PBE) [29]. DFT+ U on-site potentials [30] were
130 included for Gd- $4f$ orbitals with $\underline{U}_{\text{eff}} = 6\text{eV}$ [31]. Traditional DFT underestimates band seriously
131 in general and hence is not able to make accurate predictions for the relative energy levels [32].
132 To solve this problem, we employed hybrid functional PBE0 [33] and GW approximation [34]
133 to determine the band gaps and the positions of Ce^{3+} $4f$ and $5d$ levels. The crystal structure of
134 the $\text{RE}_3\text{Al}_5\text{O}_{12}$ (RE = rare earth) prototype is body centered cubic of space group Ia-3d with 160
135 (80) atoms in the cubic conventional (primitive) cell [35]. Experimental evidence shows that the
136 substitutional Ga_{Al} can occupy both octahedral (16a) and tetrahedral (24d) sites. We performed
137 calculations on both “ordered” GGAG in which the Ga atoms only occupy 24d sites and
138 160-atom special quasi-random structure (SQS) [36] with fixed Ga/Al ratio (1:1 on 16a and 2:1
139 on 24d) [37] to simulate the complex. The Ce levels are simulated by one Ce_{Gd} impurity in the

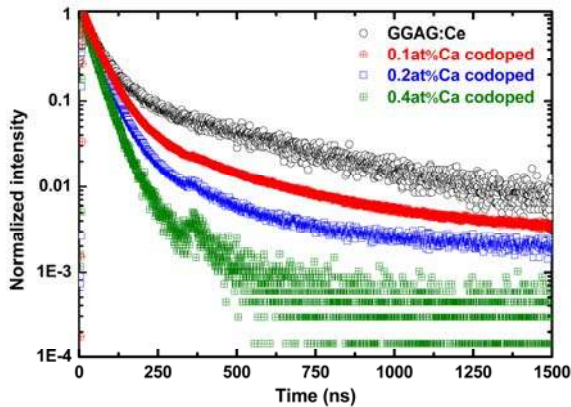
140 160 atom cell. GW approximation was applied on top of GGA+U wavefunctions. The Ce^{4+}
 141 impurity is simulated by removing one electron from the cell, and a negative background
 142 electron density is added to the system. The kinetic cut-off energy was 500 eV. Calculations
 143 sampling the gamma-point only were performed but the calculations converge within 1
 144 meV/atom. A self-consistency convergence tolerance of 1×10^{-6} eV was used for all calculations
 145 and the structures were relaxed until all the force components became less than the 0.01 eV/Å.
 146 The volumes of the lattices were relaxed with the shape of the cells fixed as cubic.

147

148 III. RESULTS AND DISCUSSION

149 A. Phenomenon: scintillation decay time shortening after Ca^{2+} codoping

150 Scintillation decay curves at room temperature are shown in FIG. 1 for GGAG:Ce and
 151 Ca^{2+} -codoped GGAG:Ce single crystals. All decay curves are approximated by two exponentials,
 152 corresponding to the prompt and delayed radiative recombination at the Ce^{3+} centers [12]. The peak at
 153 370 ns is thought to be an experimental artifact. The decay components determined from a fit of the
 154 experimental data to a two exponential function are listed in TABLE II for all four samples. The most
 155 important observation is the continuous shortening with increasing Ca^{2+} concentration of both the
 156 prompt and delayed radiative recombination components, similar to the cases of Ca^{2+} -codoped LSO:Ce
 157 single crystal [9], Mg^{2+} -codoped LuAG:Ce optical ceramic [11] and single crystal [12]. Specifically,
 158 the fast component decreases from 50 ns for uncoded sample to 22 ns for 0.4 at% Ca codoped
 159 sample, and the slow component in the 0.4 at% Ca codoped sample is an order of magnitude faster than
 160 the non-codoped sample. However, the decay components in GGAG with Ba^{2+} and B^{3+} codoping
 161 become slower than in non-codoped samples [22].



162

163 **FIG. 1** Scintillation decay profiles of GGAG:Ce and Ca^{2+} -codoped GGAG:Ce single
 164 crystals under ^{137}Cs γ -ray source excitation at room temperature.

165
166
167

TABLE II. Scintillation decay time components of GGAG:Ce doped with different Ca^{2+} concentration and the corresponding percentage of the total scintillation output.

| Compositions | Decay components | |
|-------------------|------------------|-----------|
| | Fast (ns) | Slow (ns) |
| GGAG:Ce | 50 (50%) | 372 (50%) |
| GGAG:Ce,0.1at% Ca | 45 (73%) | 226 (27%) |
| GGAG:Ce,0.2at% Ca | 40 (78%) | 137 (22%) |
| GGAG:Ce,0.4at% Ca | 27 (59%) | 59 (41%) |

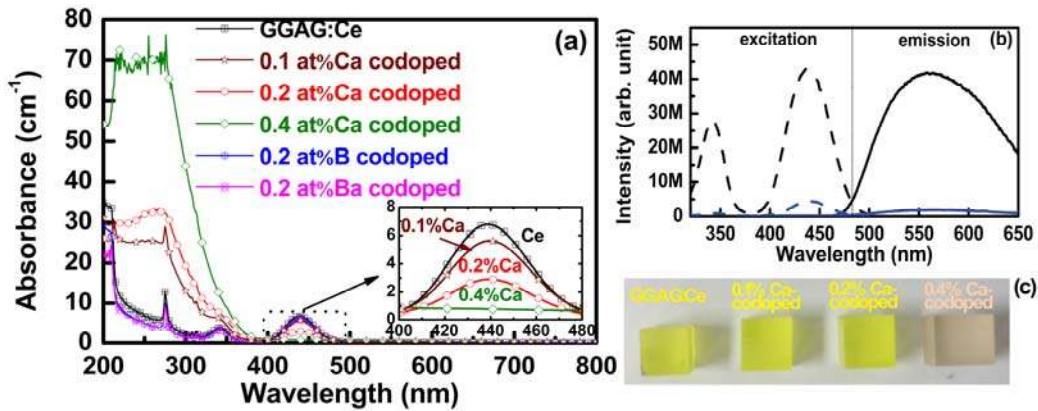
168

169 **B. Evidence of increased Ce^{4+} percentage**

170 Optical absorption spectra of Ca^{2+} codoped GGAG:Ce single crystals are plotted in FIG. 2(a) as
171 well as the spectra for B^{3+} and Ba^{2+} codoped GGAG:Ce. The $4f \rightarrow 5d_{1,2}$ transitions of Ce^{3+} centered at
172 340 and 438 nm, and the Gd^{3+} $4f \rightarrow 4f$ transition ${}^8\text{S}_{7/2} \rightarrow {}^6\text{I}_{3/2}$ at 275 nm [38] can be observed in
173 GGAG:Ce. The B^{3+} or Ba^{2+} codoped samples show similar absorption features. Ca^{2+} codoping
174 significantly changes the absorption features. The intensity of the $4f \rightarrow 5d_1$ absorption band shows a
175 decreasing trend after Ca^{2+} codoping, and almost vanishes when the Ca^{2+} codoping concentration
176 reaches 0.4 at%. It implies that the fraction of cerium that is in trivalent form is negligible. Furthermore,
177 the absorbance of Ca^{2+} codoped GGAG:Ce increases in the region of 200-370 nm compared to
178 GGAG:Ce. A similar broad absorption band peaking at around 260 nm has been ascribed to the charge
179 transfer (CT) transition from the O^{2-} levels to the Ce^{3+} ground state in Mg^{2+} -codoped LuAG:Ce [11]
180 and Ca^{2+} -codoped LYSO:Ce [10,39]. The remarkable enhancement of CT absorption intensity with
181 increasing Ca^{2+} concentration indicates an increase in the stable Ce^{4+} fraction, which is consistent with
182 the decreasing intensity of the $4f \rightarrow 5d_1$ absorption of stable Ce^{3+} . The driving force of the formation of
183 Ce^{4+} is achievement of the charge compensation required when divalent Ca ions locate at trivalent Gd
184 sites. It should be noted that divalent Ba^{2+} codoping does not show the same effect as Ca^{2+} codoping.
185 We assume that this is due to a very low concentration of Ba^{2+} in the lattice due to its much larger ionic
186 radius, which is about 142 pm for the octa-coordinated site. In comparison, Gd^{3+} is 105.3 pm and Ca^{2+}
187 is 112 pm [40].

188 Excitation spectra are much more sensitive to a trace presence of the emission center than are
189 absorption spectra. Consequently, one can detect the center existence via emission spectroscopy, even
190 when it is practically invisible in absorption. To determine if Ce^{3+} is present in a 0.4 at% Ca^{2+} codoped
191 GGAG:Ce sample, its photoluminescence excitation and emission were measured; the spectra are
192 shown in FIG.2(b). Under identical measurement conditions we observe that the $\text{Ce}^{3+} 4f \rightarrow 5d_{1,2}$

193 excitation peaks at 340 nm and 438 nm and the $5d \rightarrow 4f$ emission peak at 550 nm are very weak in 0.4 at%
 194 Ca^{2+} codoped GGAG compared with GGAG:Ce, and the integrated PL intensity in the Ca^{2+} codoped
 195 sample is at least one order of magnitude lower than that of non-codoped GGAG:Ce. This indicates that
 196 the Ce^{3+} is at a trace level in the 0.4 at% Ca^{2+} codoped sample. It is worth mentioning that when grown
 197 under the same conditions, the 0.4 at% Ca codoped GGAG:Ce single crystal is a red-brown color,
 198 which is completely different from the yellow color of GGAG:Ce single crystals codoped with other
 199 Ca^{2+} concentrations (see FIG.2(c)).

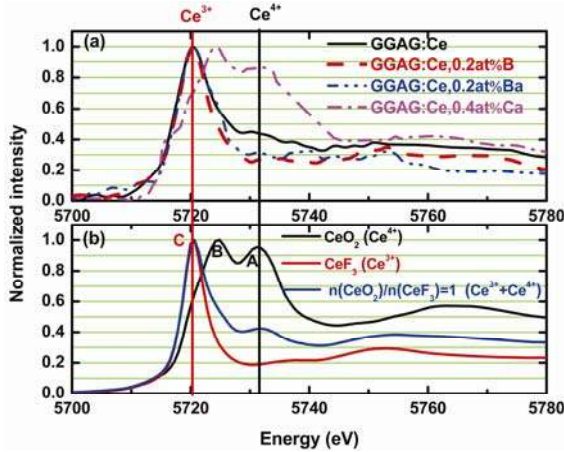


200

201 **FIG. 2** (a) Optical absorption spectra of GGAG:Ce, GGAG:Ce,B, GGAG:Ce,Ba, and GGAG:Ce,Ca
 202 single crystals. The inset is a close-up view for the Ca^{2+} codoped GGAG:Ce single crystals in the
 203 400-480 nm range; (b) Photoluminescence excitation ($\lambda_{\text{em}}=550$ nm) and emission ($\lambda_{\text{ex}}=345$ nm) spectra
 204 of GGAG:Ce (black curves) and 0.4 at% Ca^{2+} -codoped GGAG:Ce (blue curves) single crystals; (c) the
 205 Ca^{2+} codoped GGAG:Ce single crystal samples.
 206
 207

In order to directly verify the variation of the cerium valence state before and after codoping,
 208 X-ray absorption near edge spectroscopy (XANES) is utilized. XANES at the Ce L_{III} -edge of
 209 GGAG:Ce and 0.4 at% Ca^{2+} codoped GGAG:Ce are presented in FIG. 3(a). XANES of B^{3+} and Ba^{2+}
 210 codoped complexes are also shown. The XANES spectra of Ce^{4+} and Ce^{3+} comparison samples
 211 recorded at the Ce L_{III} -edge are shown in FIG. 3(b). By comparing the peak shape and the edge position
 212 with the reference CeO_2 and CeF_3 samples, the valence states of cerium in these GGAG samples can be
 213 determined. Peak A is the Ce^{4+} peak with the final state $2p4f^05d^1$ and peak B is also a Ce^{4+} peak with
 214 the final state of $2p4f^15d^1$. Peak C at about 5723 eV is a Ce^{3+} peak, which is associated with the $2p4f^15d$
 215 dipole allowed transition [41]. The XANES data from the GGAG:Ce single crystal indicates that it is a
 216 mixture of about 50% Ce^{3+} and 50% Ce^{4+} , as can be seen by comparison with the mixed reference
 217 sample. This is quite different than the pure Ce^{3+} results previously reported for the case of LSO:Ce
 218 single crystals [4,42], even though the LSO and GGAG samples were grown in essentially the same
 219 growth atmosphere. The XANES data from the 0.4 at% Ca^{2+} -codoped GGAG:Ce sample shows typical

220 Ce^{4+} features. Due to the signal-to-noise limitation, the $I(\text{Ce}^{3+})/(I(\text{Ce}^{3+})+I(\text{Ce}^{4+}))$ ratio cannot be derived
 221 by the linear combination fitting method. However, when considering the area under the $4f-5d_1$
 222 transition of Ce^{3+} in the Ca-free and 0.4 at% Ca^{2+} -codoped samples (see FIG. 2(b)), the Ce^{3+} fraction in
 223 0.4 at% Ca^{2+} -codoped sample can be estimated to be approximately 4%. Thus, the practical Ce^{3+}
 224 concentration in the 0.4 at% Ca^{2+} codoped GGAG crystal is roughly estimated to be less than 6 ppmw,
 225 given an initial cerium concentration of 458 ppmw and an effective distribution coefficient of 0.322 for
 226 cerium ions in GGAG [21], and a Ce^{3+} ratio of 4%. So far, only $\text{SiO}_2:0.01$ mol% Ce sintered in an
 227 oxidizing atmosphere has been reported to contain 100% of Ce^{4+} as measured via absorption spectra
 228 [43]. Examination of the shoulder corresponding to peak A for B^{3+} or Ba^{2+} codoped samples reveals an
 229 apparent reduction in absorption intensity, consistent with decreasing Ce^{4+} content. This phenomenon is
 230 in good agreement with the changes in the CT absorption when compared with the GGAG:Ce.
 231 Therefore, the phenomena described above imply a close correlation between scintillation response
 232 acceleration and tetravalent cerium concentration increase.



233
 234 **FIG. 3** (a) Ce L_{III}-edge XANES spectra of GGAG:Ce, GGAG:Ce,0.2 at% B^{3+} , GGAG:Ce, 0.2 at%
 235 Ba^{2+} , and GGAG:Ce,0.4 at% Ca^{2+} single crystals; (b) The XANES spectra of the Ce^{4+} and Ce^{3+}
 236 standard samples recorded at Ce L_{III}-edge are used as references.
 237

238 C. Energy level diagram construction

239 To shed light on the luminescence behaviors, we constructed the energy level diagrams of Ce^{3+}
 240 and Ce^{4+} in GGAG by the three-parameter method based on E_{4f-5d1} and E_{CT} for Ce^{4+} , and E_{4f-5d} and E_{cd}
 241 for Ce^{3+} , and E_g . We present the results from first principles calculations. The calculated lattice
 242 constants and bandgaps for $\text{Gd}_3\text{Al}_5\text{O}_{12}$ (GAG), ordered GGAG, and SQS-GGAG are listed in TABLE
 243 III. Experimental results are also listed for comparison. Both functionals overestimate the lattice
 244 constants. PBE0 predicts smaller deviation of the lattice constant from experiment. The SQS structure

245 is predicted to have smaller lattice constants compared to ordered GGAG. Similar results were obtained
 246 in Ref. [45]. Accordingly, higher bandgaps are predicted for SQS-GGAG. The bandgap is significantly
 247 reduced (~ 0.7 eV from PBE0) by Ga doping in the original GAG crystals, consistent with the
 248 “bandgap engineering” mechanism in Ref. 16. Based on the exciton energy (E_{exciton}) for GGAG
 249 reported in Ref. [44] and the rule of thumb $E_g=1.08 \times E_{\text{exciton}}$ [44]), E_g is calculated to be 6.8 eV as
 250 listed in TABLE III. Use of the PBE0 functional produces a bandgap (6.4 eV) matching experimental
 251 prediction closely.

252 **TABLE III.** Calculated lattice constants (a) and bandgaps (E_g) of GAG, ordered GGAG and
 253 SQS-GGAG using different functionals.

| | GAG | | GGAG-ordered | | GGAG-SQS | |
|-------|---------------------|--------------------|--------------|------------|---------------------|-------------|
| | a (Å) | E_g (eV) | a (Å) | E_g (eV) | a (Å) | E_g (eV) |
| GGA+U | 12.20 | 3.96 | 12.41 | 3.62 | 12.40 | 3.64 |
| PBE0 | 12.11 | 7.16 | 12.30 | 6.35 | 12.28 | 6.40 |
| Expt. | 12.11 ^{a)} | 7.07 ^{b)} | - | - | 12.27 ^{c)} | ~ 6.80 |

254 ^{a)} Derived from Powder Diffraction File for $\text{Gd}_3\text{Al}_5\text{O}_{12}$ (PDF 73-1371);

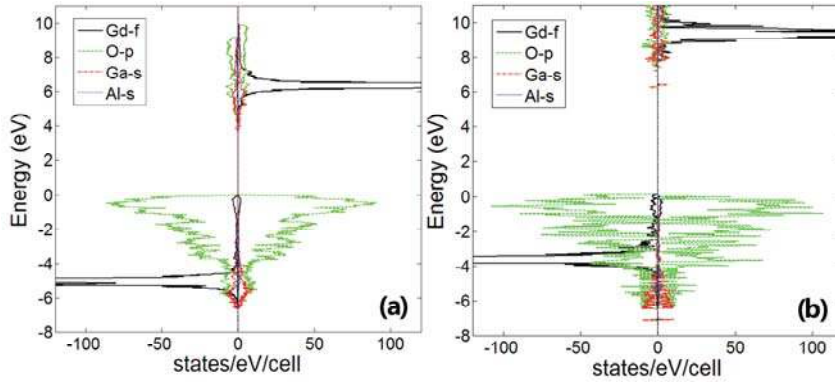
255 ^{b)} Derived from Ref. 44;

256 ^{c)} See supplemental material I.

257 The partial density of states (PDOS) of SQS-GGAG calculated by GGA+U and PBE0 is shown in
 258 FIG. 4. The plot shows the PDOS for two different spin states indicated by positive and negative values.
 259 The top of the valance band consists mainly of O $2p$ states and the conduction band minimum (CBM)
 260 consists of Ga $5s$ states. Based on our PBE0 results, there is a significant splitting between the two spin
 261 states of the Gd $4f$ orbitals. The first spin state accommodates all 7 $4f$ electrons of Gd and is 3.5 eV
 262 below the VBM. The other spin state of Gd $4f$ orbitals are unoccupied, lying at 2.5 eV above CBM.
 263 The CBM Ga $5s$ states calculated by the PBE0 functional shown in FIG. 3 are more localized compared
 264 to GGA+U results, however, it is a nonphysical result introduced by insufficient K-mesh sampling. The
 265 PDOS results from the PBE0 functional were constructed by using a $2 \times 2 \times 2$ K-mesh because of
 266 exceedingly high computational complexity when using more refined K-mesh sampling with PBE0
 267 functional. We performed DFT+ G_0W_0 calculations to make the most accurate predictions for the
 268 energy levels. The positions of the lowest $4f$ and $5d$ levels of Ce relative to VBM/CBM for Ce^{3+} and
 269 Ce^{4+} are shown in FIG. 5(a). The band gap calculated using G_0W_0 is 6.63 eV, which is even closer to
 270 the experimental evaluation compared to PBE0 hybrid functional results (6.40 eV). Both of the lowest
 271 $4f$ and $5d$ levels of Ce lie inside the forbidden gap of the host crystal. The $4f \rightarrow 5d_1$ transition energy is
 272 quite close, being 2.68 eV and 2.65 eV respectively in Ce^{3+} and Ce^{4+} . A previous ab-initio calculation
 273 based on quantum cluster approaches predicted the $4f \rightarrow 5d$ transition of 23927 cm^{-1} (2.97 eV) for
 274

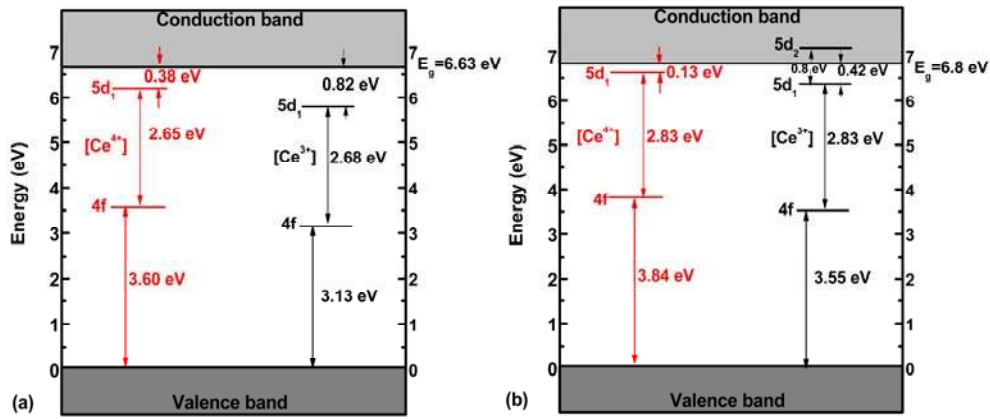
275 $\text{Ce}_Y, \text{Ga}_{\text{Al}}^{\text{oct}}$:YAG systems [46]. By localizing a hole at the Ce_{Gd} site, the lowest Ce $4f$ level becomes
276 unoccupied and the $4f$ -VBM gap increased from 3.13 eV to 3.60 eV. Correspondingly, the lowest 5d
277 level in Ce^{4+} is pushed up toward the CBM, leaving a $5d$ -CBM gap of 0.38 eV compared to 0.82 eV in
278 Ce^{3+} . Based on the calculation results, the theoretical energy level diagrams of Ce^{3+} and Ce^{4+} are
279 constructed and plotted in FIG. 5(a).

280 As shown in FIG. 2(a), E_{CT} seems to be within 3.35-3.18 eV (370-390 nm). However, the accurate
281 estimation of the onset of CT absorption of Ce^{4+} (E_{CT}) is influenced by the existence of an additional
282 excitation band between 3.54 and 3.26 eV (350-380 nm) in Ca^{2+} codoped GGAG:Ce [23]. Based on its
283 fast PL decay time of 3.6 ns and a small Stokes shift of 0.4 eV, along with its correlation with
284 atmosphere annealing, the absorption band is related to F^+ centers (positively charged oxygen vacancies)
285 [23], which was also shown in La^{3+} doped LuAG single crystals [47] and undoped LuAG single
286 crystals [48]. By analysis of the results of annealing Ca^{2+} codoped GGAG:Ce in air atmosphere, e.g.
287 0.2 at% Ca codoped GGAG, the influence of the absorption band associated with F^+ center can be ruled
288 out and the authentic onset of CT absorption of Ce^{4+} can be estimated to be 323 nm (3.84 eV) [22],
289 which shifts to the higher energy side in comparison to the E_{CT} of 3.65 eV (340 nm) for LuAG:Ce,Mg
290 [11] and 3.65-3.54 eV (340-350 nm) for LYSO:Ce,Ca/Mg [10,39]. E_{cd} for Ce^{3+} , the energy separation
291 between the $5d_I$ state of Ce^{3+} and the conduction band, was reported to be 0.42 eV [22]. We recall that
292 the E_{4f-5d_I} for Ce^{3+} is 2.83 eV (438 nm) (see FIG. 2). Under the assumption of comparable Stokes shift
293 the E_{4f-5d_I} value for Ce^{4+} is assumed to be the same as that of Ce^{3+} owing to identical radioluminescence
294 emissions (See FIG.7) [10]. On the basis of the above optical parameters, the experimental energy level
295 diagrams of Ce^{3+} and Ce^{4+} in GGAG host were constructed and plotted in FIG. 5(b). The deviation
296 between E_{CT} and E_{Vf} (the energy separation between the top of VB and the $4f$ ground state of Ce^{3+}) is
297 within 0.5 eV, which suggests the Coulomb interaction between the electron transferred to Ce^{3+} ions
298 and the hole kept at O^{2-} ions does compensate for the relaxation energy of charge transfer state [24]. It
299 is worth noticing that these energy level positions are in good agreement with the theoretical
300 calculation results, although slight differences in their absolute values exist. It is apparent that in both
301 diagrams the $4f \rightarrow 5d_I$ transition energies are equal for Ce^{3+} and Ce^{4+} , and the Ce^{4+} $5d_I$ state locates in a
302 higher position in the forbidden gap in comparison to that of Ce^{3+} .



303

304 **FIG. 4** Calculated partial density of states of 160 atom SQS of GGAG using GGA+U (a) and PBE0 (b)
 305 functionals. Positive/Negative values represent two different spin states.
 306



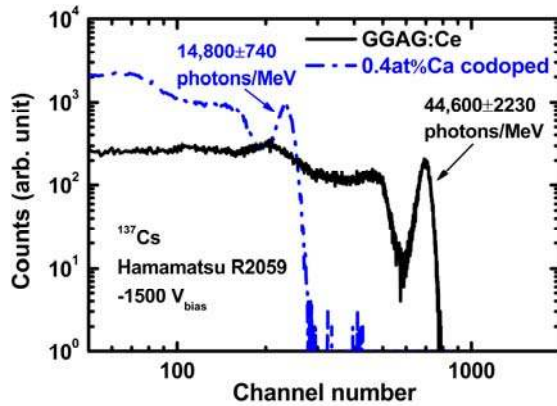
307

308 **FIG. 5** Schematic energy level diagrams of Ce^{3+} and Ce^{4+} centers in the GGAG:Ce host: (a) theory
 309 (DFT+ G_0W_0); (b) experiment (three-parameter method).
 310

311 **D. Modeling Ce^{4+} emission**

312 To prove that the scintillation occurs from Ce^{4+} , pulse height measurements under ^{137}Cs
 313 gamma-ray source excitation were made of both of 0.4 at% Ca^{2+} codoped GGAG:Ce, a sample
 314 containing negligible Ce^{3+} , and non-codoped GGAG:Ce; results are shown in FIG. 6. Using the data
 315 from the radioluminescence spectra, the emission weighted quantum efficiency (EWQE) of the R2059
 316 PMT was found to be 10% for both samples. The light yield of the 0.4 at% Ca^{2+} codoped sample is
 317 estimated to be $14,800 \pm 740$ photons/MeV, about one third of that in GGAG:Ce ($44,600 \pm 2230$
 318 photons/MeV). In general, the featured photoluminescence excitation (or absorption) and emission
 319 bands of Ce^{3+} can be observed even though its content is at trace levels [49,50], but it is not sufficient
 320 to account for all of the measured photons. Therefore, Ce^{4+} ions must play a vital role in the
 321 scintillation emission. Sr_2CeO_4 is one of the rare materials in which Ce^{4+} luminescence has been
 322 reported, and in this material the emission was assigned to a ligand-to-metal CT transition of Ce^{4+}

323 [51,52]. However, as for 0.4 at% Ca^{2+} codoped GGAG:Ce, an almost pure Ce^{4+} sample, Ce^{3+} emission
 324 peaks observed under X-ray excitation (see FIG. 7) and a fast decay time in the ns scale under γ -ray
 325 excitation (see FIG. 1) indicate that the Ce^{4+} emission model cannot be assigned to a CT emission, but
 326 another physical process through an intermediate Ce^{3+} state. Rotman et al. [53] reported that at high
 327 Ca^{2+} concentration codoping in garnets the Ce^{3+} centers completely converted into stable Ce^{4+} , but did
 328 show typical Ce^{3+} luminescence under accelerated electron excitation in cathodoluminescence spectra.
 329 It was explained by an immediate capture of electrons from the conduction band (CB) by stable Ce^{4+}
 330 centers which give rise to the excited Ce^{3+} centers and their typical emission afterwards. Similar
 331 models have been recently proposed in silicate and garnet scintillators [10,11].



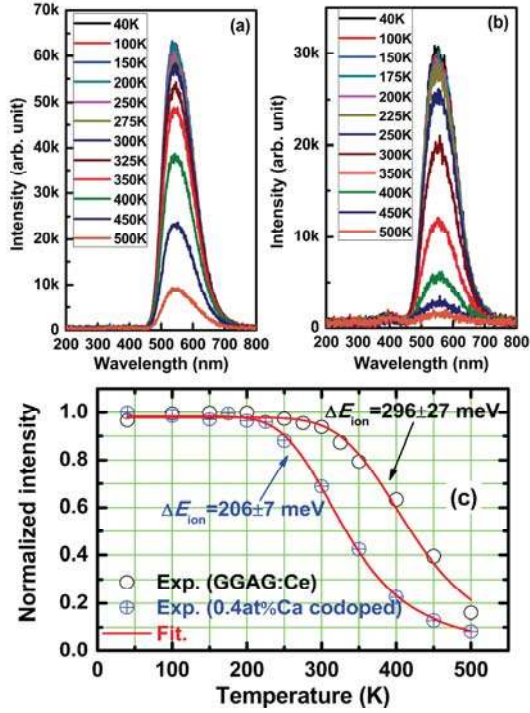
332
 333 **FIG. 6** Pulse height spectra of 662 keV γ -ray detected in GGAG:Ce and 0.4 at% Ca^{2+} codoped
 334 GGAG:Ce single crystals obtained with a Hamamatsu R2059 PMT.
 335

336 Since for Ce^{3+} thermal ionization to the conduction band is negligible around room temperature
 337 (its onset is indicated at 310 K in [19]), a difference is expected with Ce^{4+} due to its higher $5d_1$ position
 338 in the forbidden gap. In order to further corroborate the applicability of the physical processes of Ce^{4+}
 339 emission, the temperature-dependent radioluminescence spectra of GGAG:Ce with approximate 50%
 340 Ce^{4+} , and 0.4 at% Ca^{2+} codoped GGAG:Ce with almost pure Ce^{4+} were acquired, as plotted in FIG. 7(a)
 341 and (b). The measurements were recorded from 500 K to 40 K to avoid interference from
 342 thermoluminescence [54]. The Ce^{3+} emission was lower at higher temperatures in both cases, although
 343 to differing degrees. The integrated intensities derived from X-ray radioluminescence spectra in the
 344 region from 450 to 800 nm as a function of temperature are plotted in FIG. 7(c). The quenching of the
 345 0.4 at% Ca codoped sample starts at a lower temperature than that of GGAG:Ce, decreasing by 31%
 346 over the 300 K to 40 K range, in comparison to a 6% decrease over the same range for GGAG:Ce. This
 347 is in good agreement with the a similar measurement reported by Blahuta et al for LYSO:Ce and

348 Ca²⁺-codoped LYSO:Ce [10]. The solid curve shown in FIG. 7(c) represents a model calculation used
349 to describe thermal quenching of luminescence. The measured steady-state integrated intensity $I(T)$ can
350 be expressed as:

$$351 \quad I(T) = \frac{I_0}{1 + \Gamma_{nr}/\Gamma_r \exp(-\Delta E/kT)} \quad (1)$$

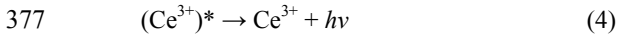
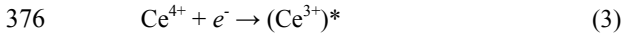
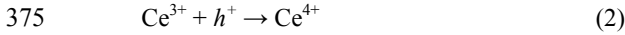
352 where $I(T)$ is the scintillation emission intensity at temperature T , I_0 the scintillation emission intensity
353 at $T=0$, and Γ_{nr} and Γ_r are the non-radiative and the radiative transition probability. ΔE is the activation
354 energy related to the ionization and/or quenching process and k the Boltzmann constant. From a fit to
355 Eq. (1) values of $\Delta E = 296 \pm 27$ meV for GGAG:Ce and $\Delta E = 206 \pm 7$ meV for 0.4 at% Ca²⁺ codoped
356 GGAG:Ce were obtained. This is consistent with the concept that the $5d_1$ position of Ce⁴⁺ is higher
357 than the $5d_1$ position of Ce³⁺ in the GGAG host and both the stable Ce³⁺ and Ce⁴⁺ ions serve as
358 luminescence centers in the GGAG host, providing the same spectra under ionizing radiation. It is
359 worth noting that these two activation energies could not be regarded as the ΔE for Ce³⁺ and Ce⁴⁺,
360 because both Ce³⁺ and Ce⁴⁺ in these two samples participate in the scintillation process under X-ray
361 irradiation. In other words, the $\Delta E = 296 \pm 27$ meV for GGAG:Ce should be underestimated for Ce³⁺,
362 and $\Delta E = 206 \pm 7$ meV for 0.4 at% Ca²⁺ codoped GGAG:Ce should be overestimated for Ce⁴⁺. In fact,
363 these two values are indeed between 0.42 eV for Ce³⁺ derived from the temperature dependent
364 photoluminescence decays (in which only Ce³⁺ ions participate) and the 0.13 eV for Ce⁴⁺ obtained from
365 the three-parameter method.



366

367 **FIG. 7** Temperature-dependent X-ray radioluminescence spectra of GGAG:Ce (a) and 0.4 at% Ca²⁺
 368 codoped GGAG:Ce (b). Their intensity variation as a function of temperature is shown in (c), and the
 369 red solid lines are fit following Eq. (1).
 370

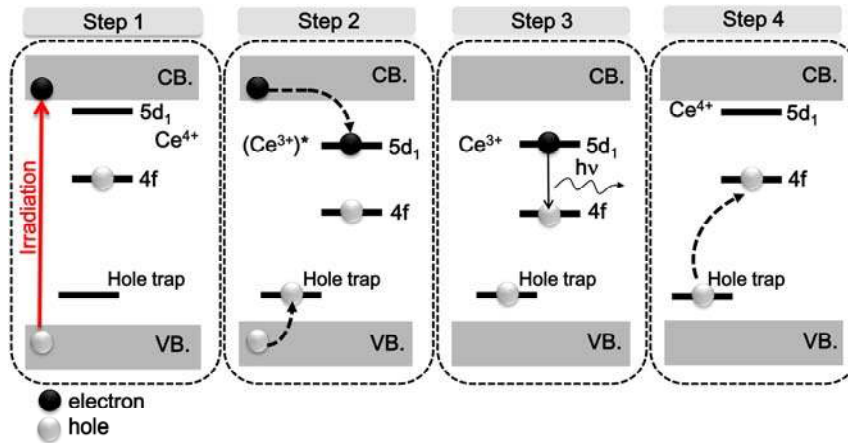
371 According to the physical processes of Ce³⁺ luminescence in scintillators [55], the scintillation
 372 process involving a stable Ce³⁺ center in the GGAG host should be creation of initial e-h pairs under
 373 ionizing irradiation, then a continuous process of capturing a hole from VB, then capturing an electron
 374 from CB, and finally radiative de-excitation followed by photon emission at around 550 nm:



378 where h^+ , e^- , $(\text{Ce}^{3+})^*$, and $h\nu$ represent an electron in CB, a hole in VB, an excited Ce³⁺ ion, and the
 379 emitted photon, respectively. It is apparent that in these three processes, the Ce⁴⁺ acts as an
 380 intermediate state. Then based on the evidence and analysis of Ce⁴⁺ emission in GGAG:Ce,Ca above, a
 381 schematic diagram of the role of stable Ce⁴⁺ in scintillation mechanism in GGAG:Ce was developed, as
 382 shown in FIG. 8. After irradiation under X-ray or γ -ray, free charge carriers (e-h pairs) are produced in
 383 the CB and VB (step 1); a stable Ce⁴⁺ ion then captures an excited electron from the CB in the empty
 384 5d energy levels and the formation of an excited $(\text{Ce}^{3+})^*$ center occurs (step 2); the Ce³⁺ emission
 385 occurs by radiative de-excitation that leaves the center in the ground state of Ce³⁺ (step 3); stable Ce⁴⁺

386 is re-created by a hole capture from the valence band or a nearby hole trap (step 4). According to Ref.
 387 52, where Ca^{2+} was introduced into garnet system, the VB hole can be trapped at neighboring oxygen
 388 ligands so that the Ce^{3+} center in the ground state (after step (3)) can thus trap a hole localized nearby
 389 the Ca^{2+} ion or a hole from VB .

390 The underlying reasons for decay time shortening by Ca^{2+} codoping in GGAG:Ce could be related
 391 to two factors: (i) a much faster emission based on stable Ce^{4+} , which is made possible by bypassing
 392 the first step of the stable Ce^{3+} scintillation mechanism under ionization irradiation, i.e. capturing a hole
 393 from VB, and a faster radiative de-excitation of the electron captured at the $5d_1$ state of Ce^{4+} because its
 394 E_{cd} is narrower than that of stable Ce^{3+} ; (ii) a more efficient energy migration of free charge carriers to
 395 activators due to the reduction in the number of shallow traps [22]. The deterioration of light yield after
 396 Ca^{2+} codoping could be related to two factors: (i) the negative consequence of the smaller E_{cd} of Ce^{4+}
 397 and (ii) formation of deep traps corresponding to the TL peaks over 300 K [22].



398
 399 **FIG. 8** Schematic diagram of the role of stable Ce^{4+} in scintillation mechanism in GGAG:Ce.

400
 401 **E. Applicability of the Ce^{4+} emission model**

402 As a practical demonstration, the Ce^{4+} emission model is applied to explain the improvement of
 403 scintillation performance in LSO:Ce,Ca [9], LYSO:Ce,Ca/Mg [10] and LuAG:Ce,Mg [11]. For the
 404 case of LuAG:Ce,Mg, the forbidden gap in LuAG is about 7.5-8.0 eV [56,57], the onset of CT is at
 405 about 3.75-3.65 eV (330-340 nm) and E_{4f-5d_1} is 2.79 eV (445 nm) [11]. Then, $5d_1$ should be at about 6.5
 406 eV above the VB edge, which means 1-1.5 eV below the CB edge, which fits the fact that $5d_2$ level in
 407 YAG was found at about 0.5 eV below CB edge [58]. The TL intensity of annealed Mg^{2+} codoped
 408 LuAG:Ce is significantly reduced in comparison to that of annealed LuAG:Ce, without formation of

409 new TL peaks [11]. Thus, after Mg^{2+} codoping in LuAG:Ce, not only was the decay time accelerated
410 by the formation of Ce^{4+} , but a combination of sufficient separation between $5d_I$ state of Ce^{4+} and CB
411 (1-1.5 eV) and traps suppression both contributed to the light yield enhancement.

412 Because of the similarity between codoped LSO:Ce and codoped LYSO:Ce, either optical or
413 scintillation properties [9,12,59,60], codoped LYSO:Ce is chosen to be discussed. Using previous
414 reports on LYSO:Ce as an example, based on an E_g of 7.4 eV, an E_{4f-5d_I} of 3.47 eV and an E_{CT} between
415 3.54 and 3.65 eV [10], the $5d_I$ state position of Ce^{4+} is 0.28-0.39 eV below the CB. It located at a
416 higher position in the forbidden gap than the $5d_I$ of Ce^{3+} ($\Delta E_{ion}=0.435$ eV) in LYSO:Ce [61]. Thus, the
417 formation of Ce^{4+} will result in unwanted thermal ionization effects in LYSO:Ce,Ca. Thanks to the TL
418 intensity reduction throughout the measured temperature range in Ca^{2+} codoped LYSO:Ce [14,60], trap
419 suppression and more efficient energy migration of free charge carriers to activators can be ensured,
420 which in turn in favors light yield enhancement and decay time shortening. Thus, the time response
421 optimization in Ce^{3+} -based scintillators for PET and TOF-PET applications can be achieved by
422 composition engineering through codoping ions with lower valence state and closer ionic radius with
423 respect to the substituted cations in matrix in order to increase the stable Ce^{4+} fraction, although at the
424 risk of light yield deterioration.

425

426 **IV. SUMMARY**

427 A correlation between the stable Ce^{4+} fraction and the Ca^{2+} codoping concentration has been
428 established, and we have shown that the fraction of the cerium that is in the stable Ce^{3+} state is
429 negligible in GGAG:Ce codoped with 0.4 at% Ca^{2+} . A higher position of the lowest $5d_I$ excitation state
430 of Ce^{4+} in the forbidden gap in comparison to that of Ce^{3+} was confirmed. A Ce^{4+} emission model at ns
431 scale under high-energy excitation was given through an intermediate Ce^{3+} state by capturing an
432 electron from CB, radiative de-excitation of Ce^{3+} and a return to the initial state by capturing a hole
433 from a nearby hole trap or the valence band. The underlying reasons for the decay time shortening by
434 Ca^{2+} codoping in GGAG:Ce are related to a much faster emission from Ce^{4+} in comparison to Ce^{3+} and
435 more efficient and faster energy migration of free charge carriers to activators. The deterioration of
436 light yield after Ca^{2+} codoping in GGAG:Ce is ascribed to the negative consequence of narrowed E_{cd}
437 for Ce^{4+} and formation of deep traps after Ca^{2+} codoping. An understanding of Ce^{4+} emission model is
438 essential for the composition engineering of the Ce^{3+} activated scintillators with fast timing response

439 needed for PET and TOF-PET applications. More comprehensive studies are presently under way in
440 which other material system will be studied.

441

442 **ACKNOWLEDGEMENTS**

443 The authors thank the Shanghai Synchrotron Radiation Facility for the use of beam time at BL14W1
444 beamline. The authors would like to gratefully acknowledge the support from Siemens Medical
445 Solutions Molecular Imaging, and that offered in part by the National Nature Science Foundation of
446 China (Grant No.51202276), Shanghai Institute of Ceramics Innovation Program (Grant
447 No.Y39ZC2130G) and Open Fund of the State Key Laboratory of Crystal Material (Grant No.KF1305).
448 Q. Li acknowledges the National Nuclear Security Administration, DNN R&D, through subcontract to
449 Lawrence Berkeley National Laboratory DE-AC02-05CH1123, and the US Department of Homeland
450 Security, DND0, under competitively awarded contract NSF ECCS-1348361. This support does not
451 constitute an express or implied endorsement on the part of the government.

452

453 **REFERENCES**

- 454 [1] S. S. Gambhir, Molecular imaging of cancer with positron emission tomography, *Nat. Rev. Cancer*
455 **2**, 683 (2002).
- 456 [2] C. L. Melcher, Scintillation crystals for PET, *J. Nucl. Med.* **41(6)**, 1051 (2000).
- 457 [3] M. J. Weber and R. R. Monchamp, Luminescence of $\text{Bi}_4\text{Ge}_3\text{O}_{12}$ - spectral and decay properties, *J*
458 *Appl. Phys.* **44**, 5495 (1973).
- 459 [4] C. L. Melcher and J. S. Schweitzer, Cerium-doped lutetium orthosilicate: a fast, efficient new
460 scintillator, *IEEE Trans. Nucl. Sci.* **39**, 502 (1992).
- 461 [5] D. W. Cooke, K. J. McClellan, B. L. Bennett, J. M. Roper, M. T. Whittaker, R. E. Muenchausen,
462 and R. C. Sze, Crystal growth and optical characterization of cerium-doped $\text{Lu}_{1.8}\text{Y}_{0.2}\text{SiO}_5$, *J. Appl.*
463 *Phys.* **88(12)**, 7360 (2000).
- 464 [6] M. Conti, State of the art and challenges of time-of-flight PET, *Phys. Medica* **25**, 1 (2009).
- 465 [7] E. Auffray, B. Frisch, F. Geraci, A. Ghezzi, S. Gundacker, H. Hillemanns, P. Jarron, T. Meyer, M.
466 Paganoni, K. Pauwels, M. Pizzichemi, and P. Lecoq, A comprehensive & systematic study of
467 coincidence time resolution and light yield using scintillators of different size, wrapping and
468 doping, *IEEE Nuclear Science Symposium Conference Record*, **N4-6**, 1 (2011).
- 469 [8] W. W. Moses, Time of flight in PET revisited, *IEEE Trans. Nucl. Sci.* **50(5)**, 1325 (2003).
- 470 [9] M. A. Spurrier, P. Szupryczynski, K. Yang, A. A. Carey, and C. L. Melcher, Effects of Ca^{2+}
471 co-doping on the scintillation properties of LSO:Ce, *IEEE Trans. Nucl. Sc.* **55(3)**, 1178 (2008).
- 472 [10] S. Blahuta, A. Bessière, B. Viana, P. Dorenbos, and V. Ouspenski, Evidence and consequences of
473 Ce^{4+} in LYSO:Ce,Ca and LYSO:Ce,Mg single crystals for medical imaging applications, *IEEE*
474 *Trans. Nucl. Sci.* **60(4)**, 3134 (2013).

- 475 [11] S. P. Liu, X. Q. Feng, Z. W. Zhou, M. Nikl, Y. Shi, and Y. B. Pan, Effect of Mg^{2+} co-doping on the
476 scintillation performance of LuAG:Ce ceramics, *Phys. Status Solidi RRL* **8(1)**, 105 (2014).
- 477 [12] M. Nikl, K. Kamada, V. Babin, J. Pejchal, K. Pilarova, E. Mihokova, A. Beitlerova, K.
478 Bartosiewicz, S. Kurosawa, and A. Yoshikawa, Defect engineering in Ce-doped aluminum garnet
479 single crystal scintillators, *Cryst. Growth Des.* DOI: 10.1021/cg501005s (2014).
- 480 [13] K. Yang, C. L. Melcher, M. A. Koschan, and M. Zhuravleva, Effect of Ca co-doping on the
481 luminescence centers in LSO:Ce single crystals, *IEEE Trans. Nucl. Sci.* **58(3)**, 1394 (2011).
- 482 [14] M. Koschan, K. Yang, M. Zhuravleva, and C. L. Melcher, A comparison of the effect of Ca^{2+}
483 codoping in cerium doped GSO with that of LSO and YSO, *J. Cryst. Growth* **352**, 133 (2012).
- 484 [15] M. Nikl, J. Pejchal, E. Mihokova, J. A. Mares, H. Ogino, A. Yoshikawa, T. Fukuda, A. Vedda, and
485 C. D'Ambrosio, Antisite defect-free $Lu_3(Ga_xAl_{1-x})_5O_{12}:Pr$ scintillator, *Appl. Phys. Lett.* **88**, 141916
486 (2006).
- 487 [16] M. Fasoli, A. Vedda, M. Nikl, C. Jiang, B. P. Uberuaga, D. A. Andersson, K. J. McClellan, and C.
488 R. Stanek, Band-gap engineering for removing shallow traps in rare-earth $Lu_3Al_5O_{12}$ garnet
489 scintillators using Ga^{3+} doping, *Phys. Rev. B* **84**, 081102(R) (2011).
- 490 [17] Y. T. Wu, J. L. Luo, M. Nikl, and G. H. Ren, Origin of improved scintillation efficiency in
491 $(Lu,Gd)_3(Ga,Al)_5O_{12}:Ce$ multicomponent garnets: An X-ray absorption near edge spectroscopy
492 study, *APL Mater.* **2**, 012101 (2014).
- 493 [18] K. Kamada, T. Yanagida, J. Pejchal, M. Nikl, T. Endo, K. Tsutumi, Y. Fujimoto, A. Fukabori, and
494 Y. Yoshikawa, Scintillator-oriented combinatorial search in Ce-doped $(Y,Gd)_3(Ga,Al)_5O_{12}$
495 multicomponent garnet compounds, *J. Phys. D: Appl. Phys.* **44**, 505104 (2011).
- 496 [19] K. Kamada, T. Endo, K. Tsutumi, T. Yanagida, Y. Fujimoto, A. Fukabori, A. Yoshikawa, J. Pejchal,
497 and M. Nikl, Composition engineering in cerium-doped $(Lu,Gd)_3(Ga,Al)_5O_{12}$ single crystal
498 scintillators, *Cryst. Growth Des.* **11**, 4484 (2011).
- 499 [20] J. A. Mares, M. Nikl, E. Mihokova, A. Beitlerova, A. Vedda, and C. D'Ambrosio, Scintillation
500 response comparison among Ce-doped aluminum garnets, perovskites and orthosilicate, *IEEE*
501 *Trans. Nucl. Sci.* **55**, 1142 (2008).
- 502 [21] K. Kamada, T. Yanagida, T. Endo, K. Tsutumi, Y. Usuki, M. Nikl, Y. Fujimoto, A. Fukabori, and A.
503 Yoshikawa, 2 inch diameter single crystal and scintillation properties of $Ce:Gd_3Al_2Ga_3O_{12}$, *J.*
504 *Cryst. Growth* **352**, 88 (2012).
- 505 [22] M. Tyagi, F. Meng, M. Koschan, S. B. Donald, H. Rothfuss, and C. L. Melcher, Effects of
506 codoping on scintillation and optical properties of a Ce-doped $Gd_3Ga_3Al_2O_{12}$ scintillator, *J. Phys.*
507 *D: Applied Phys.* **46**, 475302 (2013).
- 508 [23] F. Meng, M. Koschan, Y. T. Wu, C. L. Melcher, and P. Cohen, Relationship between Ca^{2+}
509 concentration and properties of GGAG:Ce scintillators, *IEEE Trans. Nucl. Sci.* unpublished.
- 510 [24] P. Dorenbos, Systematic behavior in trivalent lanthanide charge transfer energies, *J. Phys.:*
511 *Condens. Matter* **15**, 8417 (2003).
- 512 [25] D. Z. Ding, H. Feng, G. H. Ren, M. Nikl, L. S. Qin, S. K. Pan, and F. Yang, Air atmosphere
513 annealing effects on LSO:Ce crystal, *IEEE Trans. Nucl. Sci.* **57**, 1272 (2010).

- 514 [26] B. Ravel and M. Newville, ATHENA and ARTEMIS: Interactive graphical data analysis using
515 IFEFFIT, Phys. Scr. **115**, 1007 (2005).
- 516 [27] G. Kresse and J. Hafner, Ab initio molecular dynamics for liquid metals, Phys. Rev. B **47**, 558
517 (1993).
- 518 [28] G. Kresse and D. Joubert, From ultrasoft pseudopotentials to the projector augmented-wave
519 method Phys. Rev. B **59**, 1758 (1999).
- 520 [29] J. P. Perdew, K. Burke, and M. Ernzerhof, Generalized gradient approximation made simple, Phys.
521 Rev. Lett. **77**, 3865 (1996).
- 522 [30] S. L. Dudarev, G. A. Botton, S. Y. Savrasov, C. J. Humphreys, and A. P. Sutton,
523 Electron-energy-loss spectra and the structure stability of nickel oxide: An LSDA+U study, Phys.
524 Rev. B **57**, 1505 (1998).
- 525 [31] V. I. Anisimov, F. Aryasetiawan, and A. I. Lichtenstein, First-principles calculations of the
526 electronic structure and spectra of strongly correlated systems: the LDA+U method, J. Phys.:
527 Condens. Matter **9**, 767 (1997).
- 528 [32] Y. N. Xu, W. Y. Ching, and B. K. Briceken, Electronic structure and bonding in garnet crystals
529 $Gd_3Sc_2Ga_3O_{12}$, $Gd_3Sc_2Al_3O_{12}$, and $Gd_3Ga_5O_{12}$ compared to $Y_3Al_5O_{12}$, Phys. Rev. B **61**, 1817
530 (2000).
- 531 [33] J. P. Perdew, M. Ernzerhof, and K. Burke, Rationale for mixing exact exchange with density
532 functional approximations, Chem. Phys. **105**, 9982 (1996).
- 533 [34] L. Hedin, New method for calculating the one-particle green's function with application to the
534 electron-gas problem, Phys. Rev. **139**, A796 (1965).
- 535 [35] Y. N. Xu and W. Y. Ching, Electronic structure of yttrium aluminum garnet ($Y_3Al_5O_{12}$), Phys. Rev.
536 B **59**, 10530 (1999).
- 537 [36] A. Zunger, S.-H. Wei, L. G. Ferreira, and J. E. Bernard, Special quasirandom structures, Phys. Rev.
538 Lett. **65**, 353 (1990).
- 539 [37] See Supplemental Materials at [] for crystal data and structure refinement for $Gd_3Ga_3Al_2O_{12}$.
- 540 [38] Y. T. Wu, M. Nikl, V. Jary, and G. H. Ren, Thermally induced ionization of $5d_1$ state of Ce^{3+} ion in
541 $Gd_3Ga_3Al_2O_{12}$ host, Chem. Phys. Lett. **574**, 56 (2013).
- 542 [39] W. Chewpraditkul, C. Wanarak, T. Szczesniak, M. Moszynski, V. Jary, A. Beitlerova, and M. Nikl,
543 Opt. Mater. **35(9)**, 1679 (2013).
- 544 [40] J. A. Dean, Lange's handbook of chemistry, (15th edition) McGraw-Hill, New York (1979).
- 545 [41] C. Mansuy, J. M. Nedelec, and R. Mahiou, Molecular design of inorganic scintillators: from
546 alkoxides to scintillating materials, J. Mater. Chem. **14**, 3274 (2004).
- 547 [42] C. L. Melcher, S. Friedrich, S. P. Cramer, M. A. Spurrier, P. Szupryczynski, and R. Nutt, Cerium
548 oxidation state in LSO:Ce scintillators, IEEE Trans. Nucl. Sci. **52(5)**, 1809 (2005).
- 549 [43] M. Fasoli, A. Vedda, A. Lauria, F. Moretti, E. Rizzelli, N. Chiodini, F. Meinardi, and M. Nikl,
550 Effect of reducing sintering atmosphere on Ce-doped sol-gel silica glasses, J. Non-Cryst. Solids
551 **355**, 1140 (2009).
- 552 [44] P. Dorenbos, Electronic structure and optical properties of the lanthanide activated
553 $RE_3(Al_{1-x}Ga_x)_5O_{12}$ (RE=Gd, Y, Lu) garnet compounds, J. Lumin. **134**, 310 (2013).

- 554 [45] C. R. Stanek, C. Jiang, S. K. Yadav, K. J. McClellan, B. P. Uberuaga, D. A. Andersson, and M.
555 Nikl, The effect of Ga-doping on the defect chemistry of $\text{RE}_3\text{Al}_5\text{O}_{12}$ garnets, *Phys. Status Solidi (b)*
556 **250**, 244 (2013).
- 557 [46] A. Belén Muñoz-García and L. Seijo, Structural, electronic, and spectroscopic effects of Ga
558 codoping on Ce-doped yttrium aluminum garnet: First-principles study, *Phys. Rev. B* **82**, 184118
559 (2010).
- 560 [47] Y. Zorenko, T. Zorenko, T. Voznyak, Luminescence centers in $\text{Y}_3\text{Al}_5\text{O}_{12}:\text{La}$ single crystals, *J.*
561 *Phys.: Conf. Ser.* **289**, 012028 (2011).
- 562 [48] V. Babin, V. V. Laguta, A. Maaros, A. Makhov, M. Nikl, and S. Zazubovich, Luminescence of
563 F^+ -type centers in undoped $\text{Lu}_3\text{Al}_5\text{O}_{12}$ single crystals, *Phys. Status Solidi (b)* **248**, 239 (2011).
- 564 [49] L. Guerbous and O. Krachni, Luminescence of Ce^{3+} traces in Pr^{3+} -doped LuBO_3 and YBO_3
565 orthoborates, *Radiat. Eff. Defect Solid.* **161**, 199 (2006).
- 566 [50] P. A. Tanner, C. S. K. Mak, N. M. Edelstein, K. M. Murdoch, G. Liu, J. Huang, L. Seijo, and Z.
567 Barandiarán, Absorption and emission spectra of Ce^{3+} in elpasolite lattices, *J. Am. Chem. Soc.*
568 **125**, 13225 (2003).
- 569 [51] L. Van Pieterse, S. Soverna, and A. Meijerink, On the nature of the luminescence of Sr_2CeO_4 , *J.*
570 *Electrochem. Soc.* **147(12)**, 4688 (2000).
- 571 [52] L. Li, S. Zhou, and S. Zhang, Investigation on charge transfer of Ce^{4+} in Sr_2CeO_4 blue phosphor,
572 *Chem. Phys. Lett.* **453**, 283 (2008).
- 573 [53] S. R. Rotman, H. L. Tuller, and C. Warde, Defect-property correlations in garnet crystals. VI. The
574 electrical conductivity, defect structure, and optical properties of luminescent calcium and
575 cerium-doped yttrium aluminate garnet, *J. Appl. Phys.* **71**, 1209 (1992).
- 576 [54] B. Liu, C. S. Shi, Y. G. Wei, and J. Y. Liao, the traps effect on temperature dependence of
577 luminescence from PbWO_4 crystals, *Chem. Phys. Lett.* **362**, 296 (2002).
- 578 [55] A.J. Wojtowicz, A. Lempicki, D. Wisniewski, M. Balcerzyk, and C. Brecher, The carrier capture
579 and recombination processes in Ln^{3+} -activated scintillators, *IEEE Trans. Nucl. Sci.* **43**, 2168
580 (1996).
- 581 [56] V. Babin, K. Blazek, A. Krasnikov, K. Nejezchleb, M. Nikl, T. Savikhina, and S. Zazubovich,
582 Luminescence of undoped LuAG and YAG crystals, *Phys. Stat. Sol. (c)* **2(1)**, 97 (2005).
- 583 [57] M. Kirm, A. Lushchik, Ch. Lushchik, and G. Zimmerer, in: *Physics and Chemistry of Luminescent*
584 *Materials*, edited by C. Ronda et al., The Electrochem. Soc. Proc. Ser. PV 99-40 (The
585 Electrochemical Society, Pennington, NJ, 113-122 (2000).
- 586 [58] D.S. Hamilton, S.K. Gayen, G.J. Pogatshnik, R.D. Ghen, and W.J. Miniscalco, Optical-absorption
587 and photoionization measurements from the excited states of $\text{Ce}^{3+}:\text{Y}_3\text{Al}_5\text{O}_{12}$, *Phys. Rev. B* **39(13)**,
588 8807 (1989).
- 589 [59] B. Ferrand, B. Viana, L. Pidol, and P. Dorenbos, Low-delayed luminescence dense and rapid
590 scintillator material, U.S. Patent, No. 7,651,632 B2 (2010).
- 591 [60] B. Ferrand, B. Viana, L. Pidol, and P. Dorenbos, Dense high-speed scintillator material of low
592 afterglow, U.S. Patent 8,034,258 B2 (2010).
- 593 [61] H. Feng, V. Jary, E. Mihokova, D. Z. Ding, M. Nikl, G. H. Ren, H. Y. Li, S. K. Pan, A. Beitlerova,

594 and R. Kucerkova, Temperature dependence of luminescence characteristics of
595 $\text{Lu}_{2(1-x)}\text{Y}_{2x}\text{SiO}_5:\text{Ce}^{3+}$ scintillator grown by the Czochralski method, J. Appl. Phys. **108**, 033519
596 (2010).